

ARTICLE OPEN



A bio-inspired and self-powered triboelectric tactile sensor for underwater vehicle perception

Peng Xu^{1,7}, Jianhua Liu^{1,7}, Xiangyu Liu^{1,7}, Xinyu Wang¹, Jiayi Zheng², Siyuan Wang¹, Tianyu Chen¹, Hao Wang¹, Chuan Wang¹, Xianping Fu³, Guangming Xie⁴, Jin Tao^{5,6} and Minyi Xu¹

Marine mammals relying on tactile perception for hunting are able to achieve a remarkably high prey capture rate without visual or acoustic perception. Here, a self-powered triboelectric palm-like tactile sensor (TPTS) is designed to build a tactile perceptual system for underwater vehicles. It is enabled by a three-dimensional structure that mimics the leathery, granular texture in the palms of sea otters, whose inner neural architecture provides additional clues indicating the importance of tactile information. With the assistance of palm structure and triboelectric nanogenerator technology, the proposed TPTS has the ability to detect and distinguish normal and shear external load in real-time and approximate the external stimulation area, especially not affected by the touch frequency, that is, it can maintain stable performance under high-frequency contact. The results show that the TPTS is a promising tool for integration into grippers mounted on underwater vehicles to complete numerous underwater tasks.

npj Flexible Electronics (2022)6:25; <https://doi.org/10.1038/s41528-022-00160-0>

INTRODUCTION

Autonomous underwater vehicles (AUVs) have been developed for years owing to their outstanding applicability in various industries, and different designs of the vehicles' sensors have been developed to help AUVs accomplish specific tasks^{1–4}. These tasks include mapping the local seafloor with the aid of binocular stereo vision^{5,6}, measuring specific parameters in the water column with the aid of biosensors^{7,8}, and navigating with the aid of inertial sensors^{9–11}. Although AUVs can complete numerous tasks, they are still not an indispensable part of everyday work in the marine field. One reason for this is the lack of AUVs with tactile perception capabilities equivalent to those of marine animals. More specifically, the tactile perception capacity for dexterous and in-hand manipulation is essential for situations, where visual detection is difficult or impossible^{12,13}.

The number of tactile sensors designed specifically for marine applications is still relatively small, although existing force/torque is potentially applicable to marine measurements^{14–16}. Marine mammals with tactile receptors can sense complex stimuli from organisms' motion. Tactile perception is the main way of perceiving the surrounding environment among most aquatic and semi-aquatic taxa, especially when hunting buried invertebrates or fishes¹⁷. Moreover, seals, as well as other pinniped mammals, possess the ability to detect waterborne disturbances using their facial whiskers¹⁸. Surface otters are unique among marine mammals. Sea otters have two enhanced, complementary tactile structures that can be dexterously controlled: flexible paws and a complex array of facial whiskers. The paws may have greater functional relevance than the whiskers in sea otters when visual cues are reduced or absent¹⁹. These findings suggest that the development of animal ethology may provide the scheme for the structural design of an underwater tactile sensor. Inspired by the structure of whisker follicles^{20,21}, Beem et al. designed a

fluid motion sensor to follow underwater wake using a piezoelectric material. With the assistance of the Hall effect element, an artificial whisker was proposed to distinguish two similar textures by sensing variations in stiffness²².

To date, the triboelectric nanogenerator (TENG) has not been built with a palm-like sensor for gathering information about underwater physical objects. Noticeably, TENG-based sensors are compatible with tactile receptors because Young's modulus of soft materials typically used in triboelectric sensors is at the same level as the Young's modulus of the palms of marine mammals. Thus, TENG coupled with triboelectrification and electrostatic induction has been developed as an electromechanical energy conversion technology^{23–25}. Some triboelectric devices have the potential to be used in irregular and ultralow frequency blue energy harvesting^{26–28} and self-powered mechanical sensing^{29–31}. Moreover, self-powered triboelectric sensors have shown responses to the area of external stimuli^{32–35}, the pressure change in intrabody catheter balloons³⁶, acceleration, force, and rotational motion³⁷, and in vivo microscale movements³⁸. Based on these results, a triboelectric palm-like tactile sensor (TPTS) may provide a simple scheme for providing underwater vehicles with the ability to gather information about physical objects.

Here, we report a self-powered palm-like sensor based on contact-separation channel TENG for use in building tactile perceptual systems of underwater vehicles, as shown in Fig. 1. This sensor is composed of triboelectric sensing units, a flexible support, a fixed frame, an upper hatch cover, an elastomeric O-Ring seal, and a flexible cover. In addition, the spinous structure on the sensing unit surface, composed of interlocked hills and localized at the interface between the sensing unit and flexible support, produces a localized and high-stress concentration near the receptors, playing a pivotal role in afferent stimuli for enhanced pressure perception. The deformation of the flexible cover due to external stimuli results in contact-

¹Dalian Key Laboratory of Marine Micro/Nano Energy and Self-powered Systems, Marine Engineering College, Dalian Maritime University, Dalian 116026, China. ²Transportation Engineering College, Dalian Maritime University, Dalian 116026, China. ³School of Information Science and Technology, Dalian Maritime University, Dalian 116026, China. ⁴Intelligent Biomimetic Design Lab, College of Engineering, Peking University, Beijing 100871, China. ⁵College of Artificial Intelligence, Nankai University, Tianjin 300350, China. ⁶Silo AI, Helsinki 00100, Finland. ⁷These authors contributed equally: Peng Xu, Jianhua Liu, Xiangyu Liu. [✉]email: xiegming@pku.edu.cn; taoj@nankai.edu.cn; xuminyi@dlnu.edu.cn

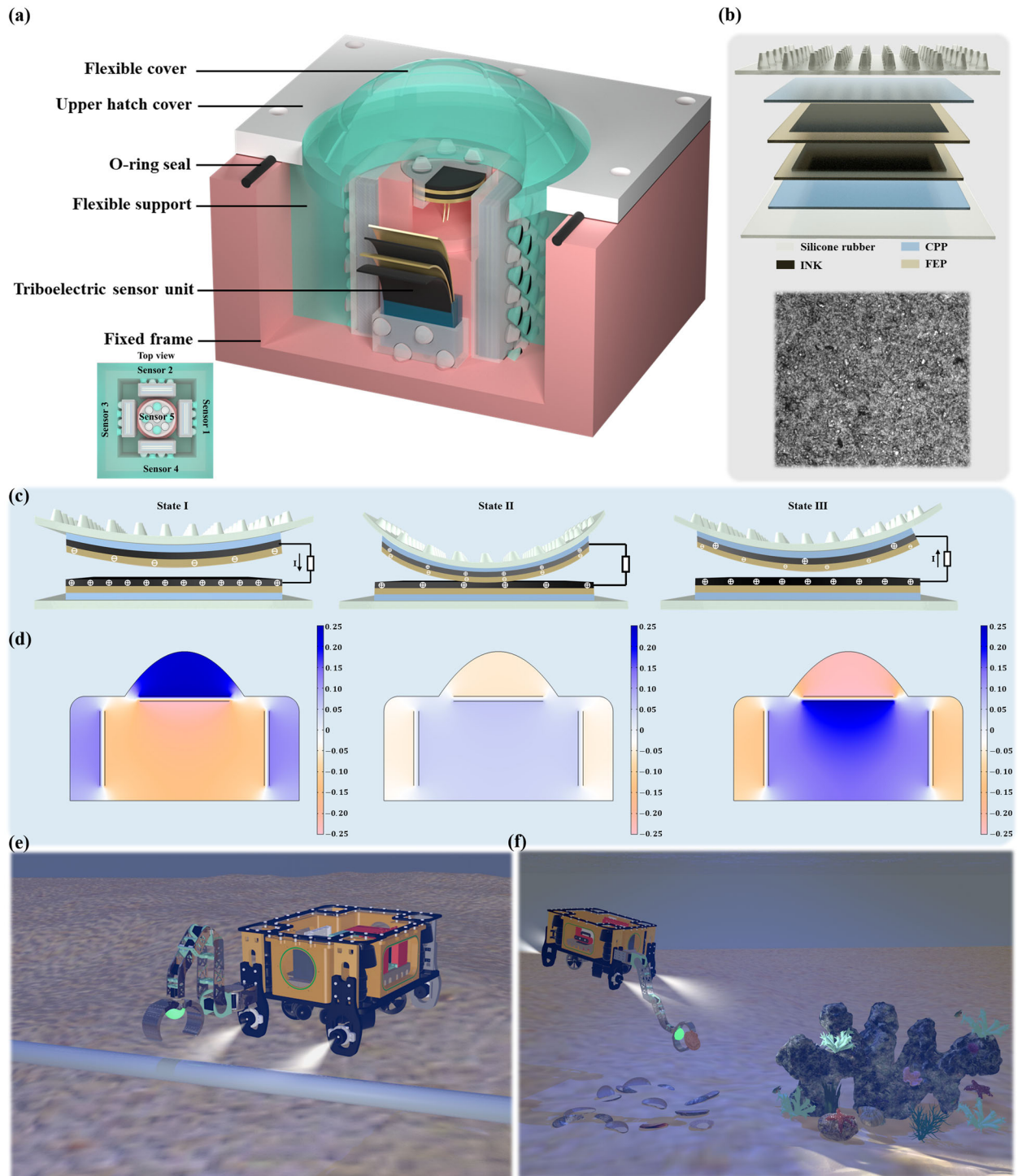


Fig. 1 The structure, working mechanism, and application of TPTS. **a** Structural diagram of TPTS. Inset: top view of the sensor unit layout. **b** Structural diagram of the sensing unit and SEM image of the FEP membrane surface. **c** Charge distribution during contact separation between FEP membrane and conductive ink. **d** Simulation of potential distribution using COMSOL software. **e** Application of the TPTS in pipeline non-destructive evaluation. **f** Application of the TPTS in underwater autonomous target grasping.

separation motion between the conductive ink layer and the fluorinated ethylene propylene (FEP) membrane for the triboelectric sensing unit, producing charge transfer over the contact electrification process. Experimental results demonstrate the potential for TPTS to be integrated into the manipulator mounted on underwater vehicles and used to complete numerous underwater tasks.

RESULTS AND DISCUSSION

Design, working principle, and simulation of TPTS

Inspired by the leathery, granular texture of sea otters' palms in ref. ¹⁹, a TPTS is designed for the tactile perception system of underwater vehicles. The function of the TPTS is to capture information about underwater targets through physical touch. Figure 1a shows the structural diagram of the tactile sensor based

on TENG. This structure consists of a triboelectric sensing unit with the spinosum structure, a flexible support, a fixed frame, an upper hatch cover, an elastomeric O-Ring seal, and a flexible cover. Specifically, the flexible cover and support (60 mm in length, 32 mm in width, and 35 mm in height) are made of silicone rubber, enabling external stimuli to be converted into sensing unit deformation. Charge transfer is generated during the deformation process. Four square sensing units (18 mm in length, 8 mm in width, and 40 mm in height) are symmetrically installed on the four inner surfaces of the square flexible support. For the sake of clarity, it is worth noting that the sensing units are counter-clockwise angles coded as 1: 0°, 2: 90°, 3: 180°, and 4: 270°. In addition, a circular-like sensing unit (8 mm in radius and 8 mm in height) is placed directly below the flexible cover, as shown in the top view of Fig. 1a.

Figure 1b depicts the structure of the triboelectric sensing unit, including silicone rubber with a spinosum structure aiming at producing a localized and high-stress concentration near receptors, a cast polypropylene (CPP) film for voiding electrostatic interference, and FEP films sprayed with conductive ink. In order to avoid contact between triboelectric layers and water, the dimension of two ink-coated FEP membranes equals the CPP membranes. Around them, there are two larger silicone layers made of Dragonskin 30 so that the silicone rubber can seal two triboelectric layers. The scanning electron microscope (SEM) image of the FEP membrane surface, depicted in Fig. 1b bottom, is characterized by a rough pattern. This nanostructure can enhance the surface charge density of the TPTS for higher sensitivity.

Figure 1c illustrates the electron transfer process of sensing units receiving external stimuli. The FEP film contacts the ink electrode, resulting in the electron clouds overlapping on the two layers. Due to FEP having greater electronegativity than ink, the electrons of the ink layer enter into the deeper potential well of the FEP film. Namely, the free electrons on the ink surface are transferred to the lowest molecular orbital at the FEP interface. When the TPTS removes an external load, the FEP film is separated from the ink electrode. Because the negative and positive friction charges no longer coincide on the same plane, a dipole moment and potential are generated between the two contact surfaces. Therefore, the free electrons are transferred through the external circuit to balance the local electric field, generating a positive charge on the conductive ink electrode. The flow of electrons continues until the distance between the two contact surfaces reaches the maximum. Meanwhile, the voltage difference decreases, and the free electrons return through the external circuit. Finally, the charge distribution returns to its initial state, which completes the whole generation cycle. As shown in Fig. 1d, COMSOL software is used to simulate the potential distribution results between the two films and verify the working principle.

Figure 1e shows the application of the TPTS for underwater pipeline non-destructive evaluation. The TPTS is installed on the end of underwater vehicles' manipulators as the pressure feedback device to prevent pipeline damage resulting from excessive clamping force. Moreover, evaluation is performed along the path of the pipeline. The damage degree of a pipeline can be obtained from the characteristics of the sensor signal. Figure 1f demonstrates the application of the TPTS for underwater autonomous target grasping. To ensure the integrity of the target, underwater vehicles need to control the magnitude of the manipulator's grasping force based on the electrical signal from the TPTS. The TPTS is regarded as a promising tool for building an underwater tactile perception system based on these applications.

Output characterization of the TPTS

In the experimental design, a linear motor and pressure sensors are used to simulate the external stimuli with different parameters.

Supplementary Fig. 7a shows the experimental setup, which is mainly composed of a linear motor, an LZ-WL2 pressure sensor with an intelligent display instrument, a Keithley 6514 electrometer, and a computer. In particular, the pressure sensor is fixed on the linear motor using a corresponding circular-like fixture. Supplementary Fig. 7b, c present photos of the experimental setup. Because all the sensing units have the same structure, only the performance of the sensing unit 1 is presented for the sake of brevity.

Figure 2a shows the deformation diagram of the sensing units under the vertical external stimuli at position (45°N, 0°E), in which the deformation of the flexible cover from the vertical external stimuli $F(t)$, with the aid of the internal flexible support, causes the triboelectric sensing unit to bend so that contact-separation motion between the conductive ink layer and FEP membrane occurs for the sensing unit. To facilitate the exhibition of experimental data, Fig. 2b shows labels on the flexible cover surface using longitude and latitude lines. Figure 2c shows that the voltage signal of the TPTS increases as the vertical external stimulus with a frequency of $f = 0.8 \text{ Hz}$ increases from 1 N to 5 N. This is because, with the help of the spinosum structure, the increasing external load results in the increasing bending magnitude of the sensing unit, which makes the contact-separation movement between the films more sufficient and generates a larger output voltage. Furthermore, the leave-one-out cross-validation (LOOCV) strategy is used to obtain the relationship between voltage and external stimuli ($U = 0.14057F + 0.05935$, $R^2 = 0.98609$) in Fig. 2d, where the correlation coefficient R^2 indicates that the external stimuli and the output voltage have an approximate linear relationship, with an error of less than 1.78% at magnitude $F = 4 \text{ N}$, and a relatively higher error of 9.40% at magnitude $F = 3 \text{ N}$. The reason for these errors may originate from the high-frequency vibration generated by the linear motor during operation and strong electromagnetic interference from the surrounding equipment. Figure 2e, f also describes the influence of external magnitude $F = 1\text{--}5 \text{ N}$ on the current signal at $f = 0.8 \text{ Hz}$. It is worth noting that the linearity between the current signal and the external load ($I = 0.58082F + 0.12191$, $R^2 = 0.99455$) is better than the linearity between the voltage signal and the external load. This result indicates that, compared to the output voltage responding to external magnitude, the output current is less affected by environmental interference.

Subsequently, under the condition of external stimuli magnitude $F = 3 \text{ N}$, sensing unit 1 is tested for voltage and current signals at different collision frequencies from 0.8 Hz to 1.6 Hz. As shown in Fig. 3a, as the collision frequency increases, the output voltage remains almost unchanged, staying around 0.58 V. It can be seen that a changing collision frequency has little effect on the voltage output of the TPTS. Figure 3b shows that the current I increases as the collision frequency increases. The linear relationship between collision frequency and current is fitted ($I = 0.45601f + 1.53521$, $R^2 = 0.98694$) in Fig. 3c. Figure 3d, e describes the relationship between the output signal (voltage and current, respectively) of the TPTS, the load magnitude, and the collision frequency. The response surface reflects the interaction between the two factors and the influence of each factor on the output signal. The shape of the equal-height line reflects the strength of the effect of the two factors. Moreover, the slope of the contour line for output current in the X - Y plane is greater than the case of output voltage, which indicates that the two factors are significant for the output current. Together with the influence of collision frequency and external load magnitude on the output signal, it is proved that the TPTS may be suitable for high-frequency sensing tasks, as it will still recognize the characteristics of the external load. For example, when the output voltage is constant and the output current continually changes, the external stimuli are characterized by time-varying frequency and constant magnitude. Finally, the durability of the TPTS is

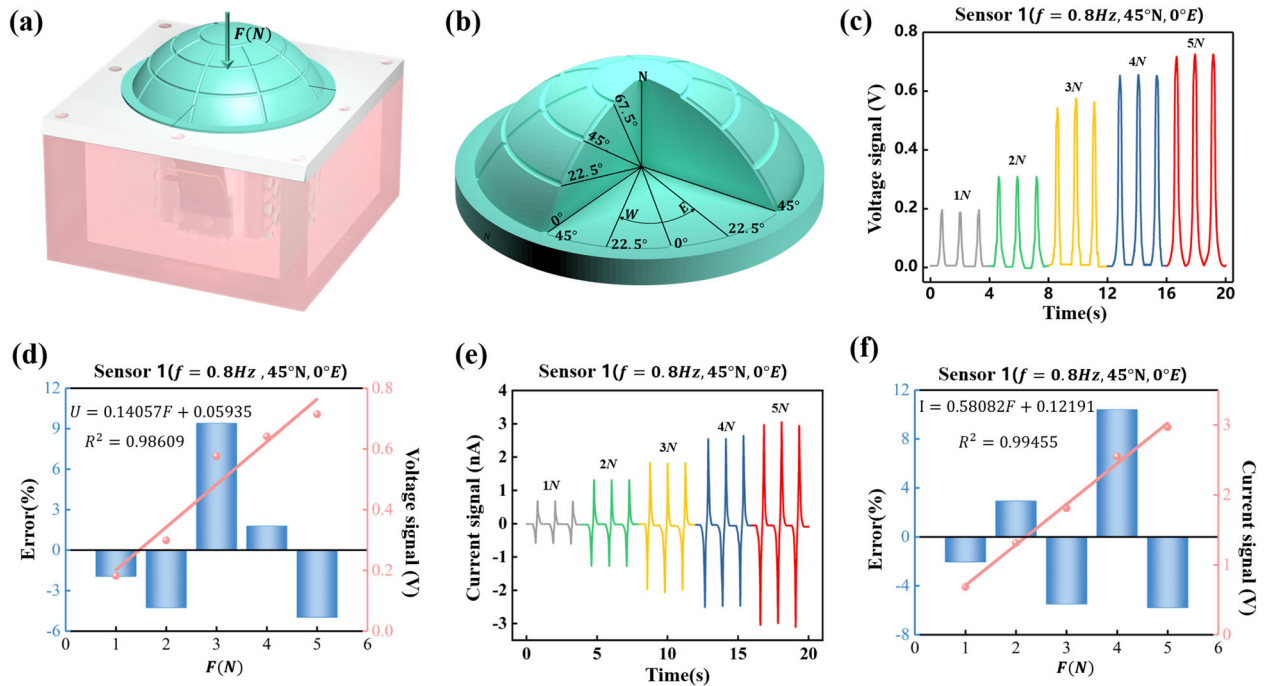


Fig. 2 The results of the TPTS excited by a linear motor. **a** Deformation diagram of sensor units under external load. **b** Labels on the flexible cover surface using longitude and latitude lines. **c** The open circuit voltage responding to external load magnitude from 1 N to 5 N. **d** Fitted linear relationship between open circuit voltage and external load magnitude. **e** The short circuit current responding to external load magnitude from 1 N to 5 N. **f** Fitted linear relationship between short circuit current and external load magnitude.

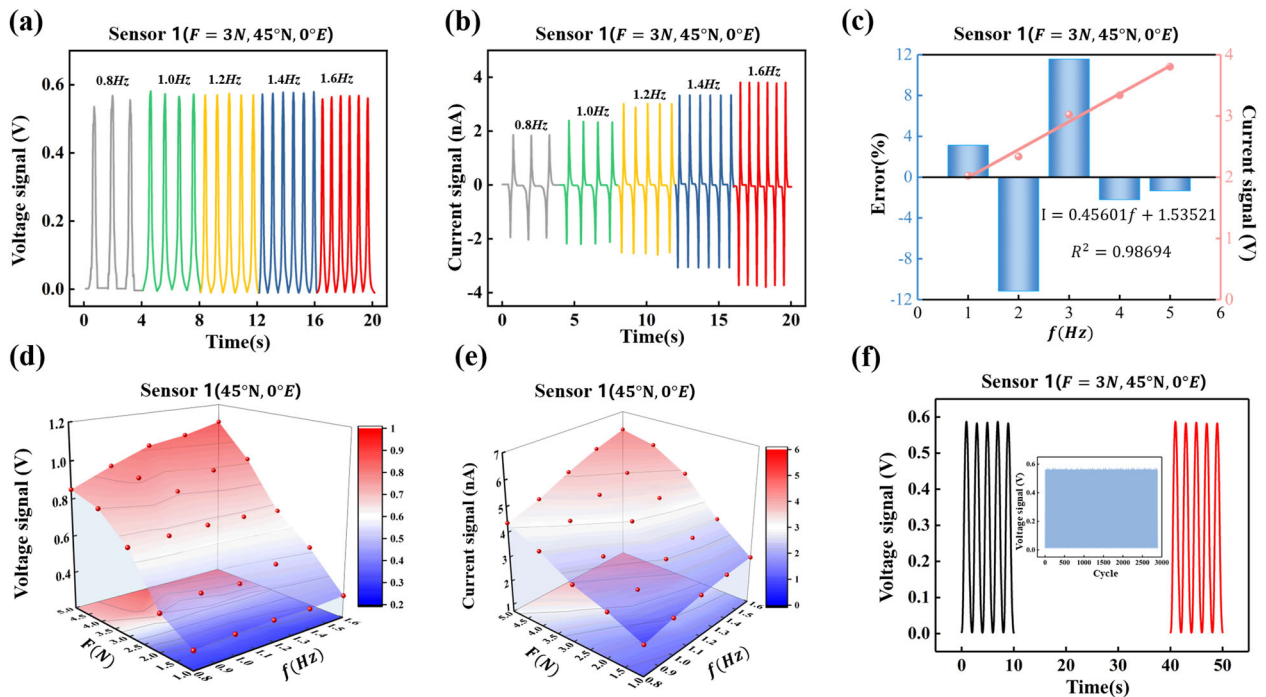


Fig. 3 Characterization of the sensing unit. **a** The open-circuit voltage responding to collision frequencies from 0.8 Hz to 1.6 Hz. **b** The short circuit current responding to collision frequencies from 0.8 Hz to 1.6 Hz. **c** Fitted linear relationship between short circuit current and collision frequencies. **d** Relationship between the output voltage of the TPTS, load magnitude, and collision frequency. **e** Relationship between the output current of the TPTS, load magnitude, and collision frequency. **f** The durability of the TPTS tested for 2800 cycles.

tested for 2800 cycles in Fig. 3f. The TPTS maintains a stable electrical signal output after repeated impacts from an external load. Since other sensing units have the same structure as sensing unit 1, similar data along the sensing units 2, 3, 4, and 5 are

plotted in Supplementary Figs. 8–10. The electronic signals are correlated with the characteristics of external stimuli for all sensing units. This indicates the sensing units can be used for signal feedback in AUV control systems.

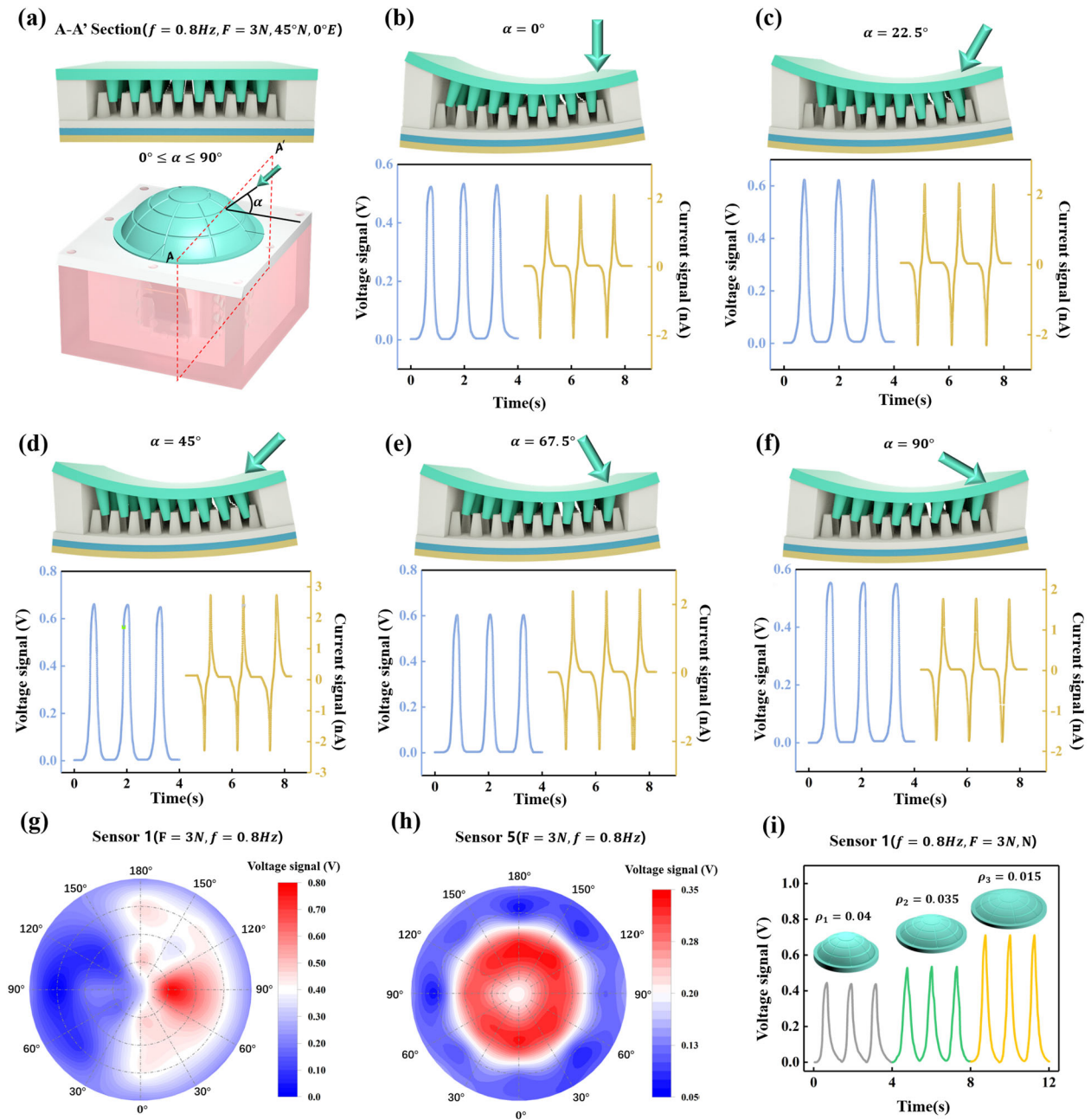


Fig. 4 Response characteristics of TPTS under different load directions and locations. **a** The initial state of triboelectric sensing unit 1, and the angle α between the external load and the horizontal line. **b** The state of sensing unit 1 at the angle $\alpha = 0^\circ$, and the open-circuit voltage and short-circuit current responding to the external load. **c** The state of sensing unit 1 at the angle $\alpha = 22.5^\circ$, and the open-circuit voltage and short-circuit current responding to the external load. **d** The state of sensing unit 1 at the angle $\alpha = 45^\circ$, and the open-circuit voltage and short-circuit current responding to the external load. **e** The state of sensing unit 1 at the angle $\alpha = 67.5^\circ$, and the open-circuit voltage and short-circuit current responding to the external load. **f** The state of sensing unit 1 at the angle $\alpha = 90^\circ$, and the open-circuit voltage and short-circuit current responding to the external load. **g** The open circuit voltage for sensing unit 1 responding to stimuli at different positions under the conditions of $F = 3\text{ N}$, $f = 0.8\text{ Hz}$, and $\alpha = 90^\circ$. **h** The open circuit voltage for sensing unit 5 responding to stimuli at different positions under the conditions of $F = 3\text{ N}$, $f = 0.8\text{ Hz}$, and $\alpha = 90^\circ$. **i** The open circuit voltage responding to flexible covers with different curvatures under the conditions of $F = 3\text{ N}$, $f = 0.8\text{ Hz}$, and $\alpha = 90^\circ$.

Interlocked hills localized at the interface between the top layer of the sensing unit and flexible support are designed to enhance pressure perception. The other key benefit of this structure is that it has the ability to detect the direction of the external load. As shown in Fig. 4a, when an external load does not press the sensing unit, the triboelectric sensing unit and the flexible support remain at the initial state. For the sake of brevity, we introduce the symbol α , ranging from 0° to 90° , as the angle between the

external stimuli and the horizontal line. Figure 4b–f depict the 3D geometry of the hills and the anisotropic deformation of the top layer with applied tilt load. For example, in the case of $\alpha = 0^\circ$, the direction of the tilt load is perpendicular to sensing unit 1, which means that no shear force is applied to the spinosum structure. Namely, the part located at position $(45^\circ\text{N}, 0^\circ\text{E})$ is only affected by the bending component. As shown in Fig. 4b, the output voltage in this state is about 0.52 V and the output current is about 2.1 nA .

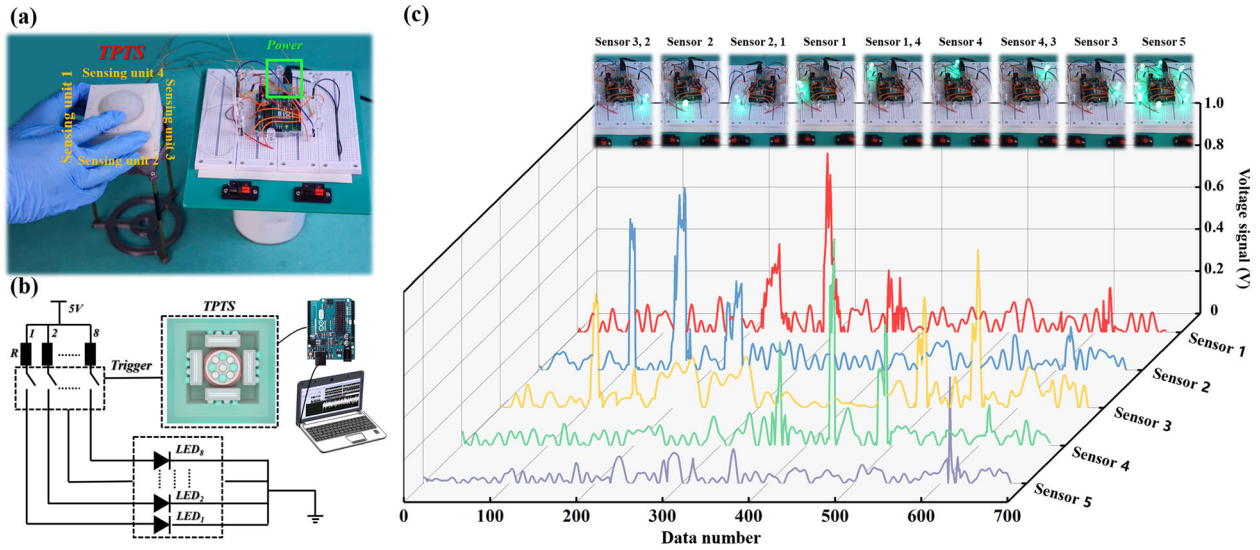


Fig. 5 Experiments with TPTS controlling LED lights. **a** Experimental electronic setup. **b** Electronic module used for potential application demonstrations, such as controlling LED lights. **c** Demonstration of TPTS as a sensitive load switch control and its corresponding output voltage signal.

In the case of $\alpha = 22.5^\circ$, the shear component and the bending component work on the part located at position $(45^\circ N, 0^\circ E)$ interactively rather than independently. As shown in Fig. 4c, the output voltage in this state is about 0.62 V and the output current is about 2.3 nA. Evidently, the shear component increases the contact interface between the top layer of the sensing unit and flexible support, which leads to a more significant increase in transfer charge compared to cases in which there is only a bending component. As α increases to 45° , the shear component causes the contact interface to interlock completely, at which time the output voltage (0.66 V) and output current (2.75 nA) reach their peak values, as shown in Fig. 4d. Figure 4e–f shows the performance of sensing unit 1 in the cases of $\alpha = 67.5^\circ$ and $\alpha = 90^\circ$, in which the shear component directions are opposite compared to the cases of $\alpha = 22.5^\circ$ and $\alpha = 45^\circ$. Thus, the output signal located at position $(45^\circ N, 0^\circ E)$ provides the ability to differentiate several types of applied external loads.

Furthermore, the TPTS can also approximate the external stimulation area based on how the output voltage responds to different position stimuli on the flexible cover surface. This functionality is amply illustrated in Fig. 4g–h via external stimuli ($F = 3\text{ N}$, $f = 0.8\text{ Hz}$, and $\alpha = 90^\circ$) applied to different positions of the flexible cover surface. From Fig. 4g, it can be observed that the magnitude of the output voltage for sensing unit 1 decreases as the applied load moves away from the center of sensing unit 1. As shown in Fig. 4h, the output voltage of sensing unit 5 is not maximized at the installation position. This is because the thickness of the flexible cover at the pole is the largest, reducing the ability to transmit load-induced deformation. As a result, the output voltage response to a load at the pole is smaller than the output voltage response to a load around the pole. Due to the similar structure and symmetrical distribution of the sensing units, the characteristic data of sensing units 2, 3, and 4 are depicted in Supplementary Figs. 11–13. Using the output voltage response to different positions, the contact centroid location can be obtained for a sphere surface of radius R in ref. ³⁹, as shown in Supplementary Fig. 2, with the following equation:

$$c = \frac{K}{K^2 + \|f\|^2} (K^2 m + Kf \times m + (f^T m)f), \quad (1)$$

where f is internal load, m denotes torque, and

$$K = \frac{-\text{sign}(f^T m)}{\sqrt{2R}} \sqrt{\zeta + \sqrt{\zeta^2 + 4R^2 (f^T m)^2}}, \quad (2)$$

$$\zeta = \|m\|^2 - R^2 \|f\|^2.$$

In addition, we also carry out performance tests using flexible covers with different curvatures. Figure 4i shows the output voltage sensing unit 1 with three flexible covers of different curvatures under the same external load ($F = 3\text{ N}$, $f = 0.8\text{ Hz}$, and $\alpha = 90^\circ$). As the curvature decreases from $\rho = 0.04$ to $\rho = 0.015$, the output voltage increases from 0.46 V to 0.73 V. This is because the smaller the curvature of the flexible cover, the smaller its thickness. The corresponding output current is shown in Supplementary Fig. 14. In the case of $\rho = 0$, the flexible cover is a plane, and the TPTS loses its ability to sense a 3D spatial load.

Real-time control

Figure 5a shows a photograph of the experimental electronic setup, wherein LEDs are installed around the TPTS at intervals of 45° , and an Arduino Due R3 is used as a circuit board to perform signal sampling and data processing. Data processing consists of two stages: system initialization and event detection via judging whether the peak voltage of the TPTS satisfies the setting value. This framework provides a triggering capability for turning on LED lights in a corresponding direction. The schematic digraph is depicted in Fig. 5b. If two sensing units are larger than the setting value at the same time, the electronic circuit drives the LED between the sensing units. The stimuli starts at the position between sensing units 2 and 3 and rotate in a clockwise manner by 45° during each step of the experiment. Figure 5b shows how the TPTS is used to control the on/off state of LED lights (also see Supplementary Video 1) by a corresponding voltage, where the peak voltage in the stimuli direction is larger than in other directions. This result indicates the TPTS' great potential in approximating the external stimulation directions.

Application of TPTS in detecting hardness

To explore the compatibility of the TPTS with underwater vehicle applications, a manipulator integrated with the TPTS and mounted on a remotely operated vehicle (ROV) is prepared to perform hardness detection of various silicone samples. As shown in Fig. 6a, b,

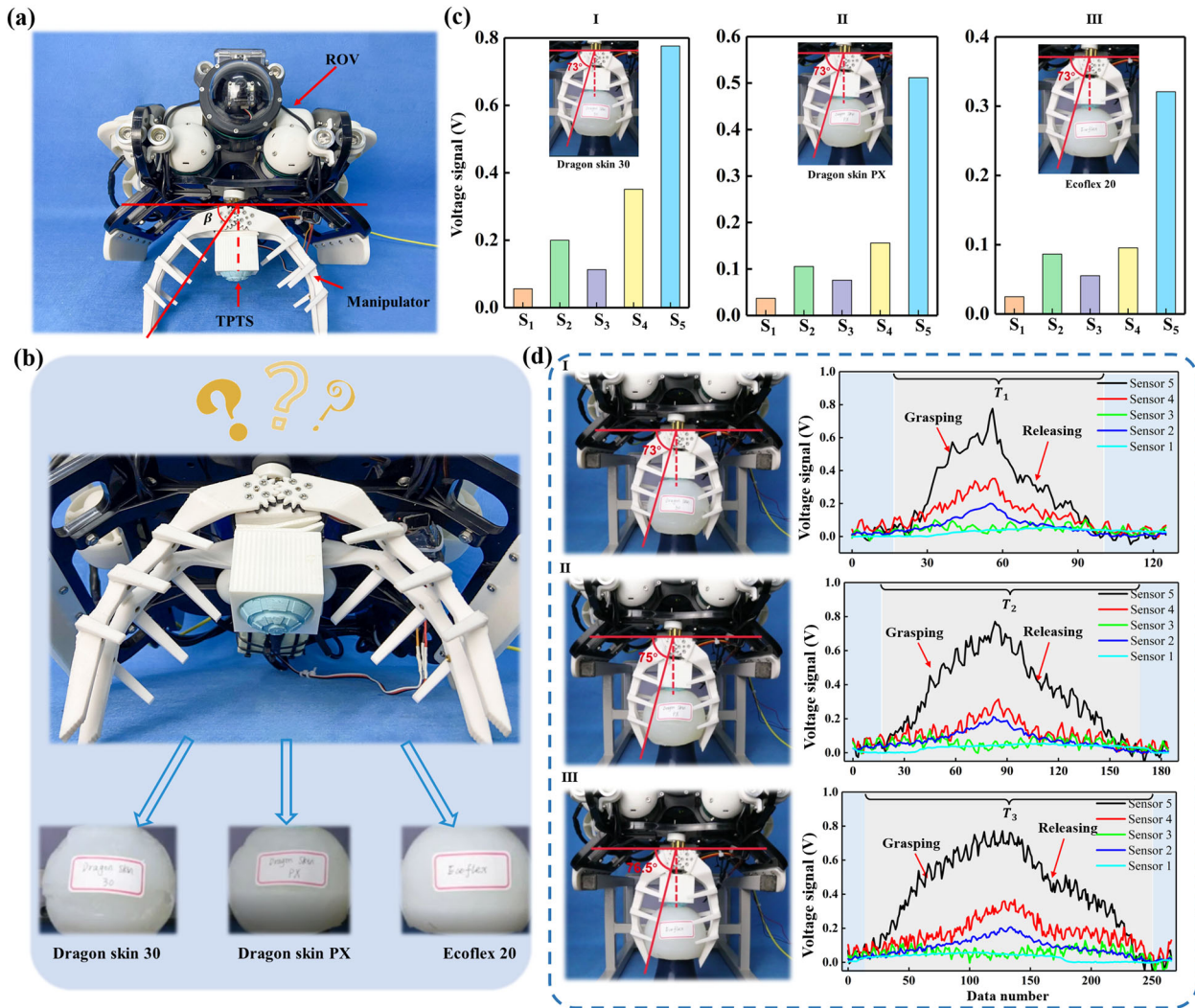


Fig. 6 Experiments with TPTS mounted on an ROV. **a, b** The configuration of the gripper and sensors for detecting the hardness of a silicone sample. **c** The output signals of the TPTS when gripping various silicone samples under the condition of $\beta = 73^\circ$. **d** Demonstration of the TPTS in a closed-loop control system for an ROV and the corresponding output voltage signal.

the TPTS is guided by bolts on the manipulator surface and is fixed at its center. To determine the relationship between the gripping angle and the output signal for various silicone samples, the gripping angle β is defined to represent the angle between the horizontal line and the gripper location. The Shore hardness of the silicone samples is 30A (Dragon skin 30), 2A (Dragon skin PX), and 00–20 (Ecoflex 20). The results show that the magnitude of flexible cover deformation increases with the incremental Shore hardness of the samples under the condition of $\beta = 73^\circ$, resulting in larger output peaks generated by the TPTS in one single actuation motion in Fig. 6c. Furthermore, when the sample with Dragon skin 30 is gripped at the palm position of the gripper, the slope of the output signal in sensing unit 5 (k_1) is higher than the others, as shown in Supplementary Fig. 15. It is worth noting that under the relatively fast gripping speed, the gripping motion can still be clearly recognized from the generated output peaks of the sensing unit (see Supplementary Video 2). In addition, the TPTS can also distinguish the gripping and releasing motions of the gripper from the rising edge and falling edge of the output signal. As a result, the slope of voltage signal increases with the incremental Shore hardness for sensing unit 5 ($k_1 > k_2 > k_3$), proving the feasibility of hardness detection with the output signals of the TPTS.

Subsequently, a simple closed-loop control system is built for grasping objects underwater, as shown in Supplementary Fig. 16.

For specific underwater objects, the desired peak voltage corresponding to the grasping force is provided, where the goal is to grasp objects without breaking them. Once the peak voltage from the TPTS reaches the setting value, the gripper will stop increasing β and maintain its current state until the object is released. For example, when grasping the sample with Dragon skin 30, the desired peak voltage is given as 0.77 V. As the output voltage reaches the setting value, the gripping motion holds on with $\beta = 73^\circ$ in T_1 , as shown in Fig. 6d (also see Supplementary Video 3). For samples with Dragon skin PX and Ecoflex 20, the gripper completes this task in T_2 and T_3 , respectively. From Fig. 6d, $T_1 < T_2 < T_3$ results from the samples with incremental Shore hardness. Therefore, different types of underwater objects may be recognized when visual cues are reduced or absent, verifying the feasibility of applying the TPTS to underwater vehicles.

Application of TPTS in non-destructive underwater pipeline evaluation

Experiments are performed in an indoor water pool (3m*2m*1.5m) with the goal of non-destructive pipeline evaluation based on the developed TPTS, as shown in Fig. 7a. For additional stability in the pool-based experiments, the pipeline (2 m in length and 5 mm in radius) with three ruptures to be detected is mounted on the floor.

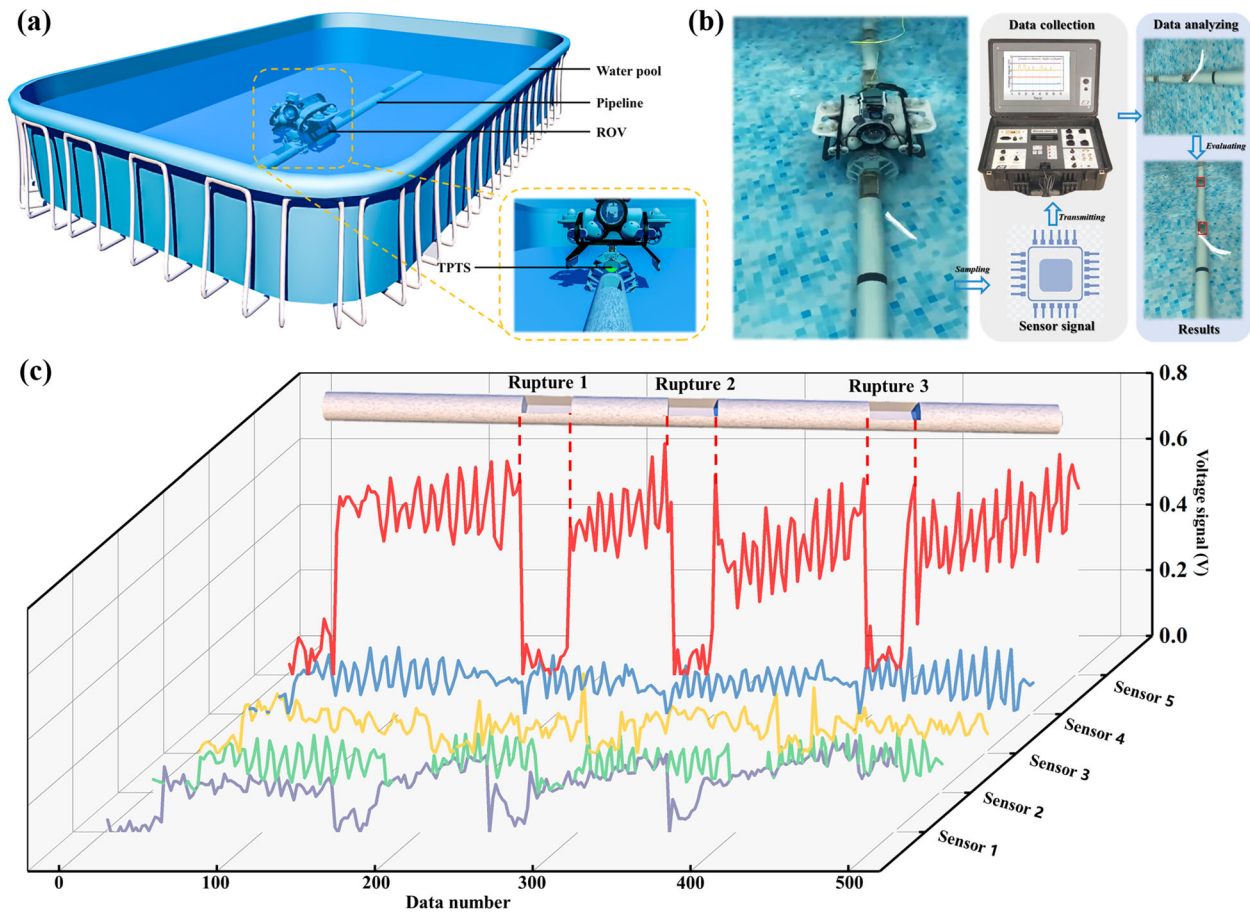


Fig. 7 Experiments with non-destructive underwater pipeline evaluation. **a** The configuration of the pipeline and sensors in use of non-destructive underwater pipeline evaluation. **b** The process flows from signal sampling to non-destructive underwater pipeline evaluation. **c** Demonstration of TPTS in non-destructive underwater pipeline evaluation and its corresponding output voltage signal.

At the beginning of the task, the ROV is operated to explore the nearby environment until the vision system detects the pipe. Subsequently, the ROV uses the manipulator to grasp the pipeline. The magnitude of the grasping force depends on whether the TPTS is in contact with the pipe. The process flow of non-destructive pipeline evaluation is depicted in Fig. 7b. After grasping the pipeline, the ROV moves forward along the pipeline until it reaches the end of the pipeline. The screen displays the real-time signals, as shown in Fig. 7c (also see Supplementary Video 5). When the presence of a falling edge stays for a period of time during the detection process, it can be judged that there is a fracture at the location of the ROV at this time. In addition, the roughness of the pipeline surface can be determined by observing the vibration magnitude of the real-time signals.

DISCUSSION

In summary, a TPTS for underwater tactile perception based on triboelectric nanogenerators is proposed and investigated in this paper. The TPTS uses the linear relationship between the output signal and parameters to sense the magnitude, frequency, and contact area of external stimuli by analyzing the contact-separation pattern and the triboelectric output of multiple sensing units. In addition, the TPTS has a spinosum structure to measure and distinguish normal and shear forces generated when interacting with an object in real time. The TPTS is then used to control the on/off states of lights oriented in various directions as

a first step toward utilizing the highly sensitive directional sensing capabilities of the TPTS. Moreover, an underwater sensory tactile system is built by mounting a manipulator integrated with the TPTS on an ROV to obtain information about grasped objects. Based on the improved intelligence of the gripper, it has the ability to detect the hardness of samples and complete grasp tasks while preventing breakage. Additionally, the underwater sensory tactile system is used to conduct non-destructive underwater pipeline evaluation, illustrating its potential future application in various fields, including underwater object monitoring and tactical surveillance.

METHODS

Fabrication of TPTS

As shown in Supplementary Fig. 17, the triboelectric sensing unit consists of six layers assembled by lamination: (i) a bottom 2 mm thick silicon substrate made of Dragonskin 30, (ii) an intermediate 1 mm thick CPP, a commercial product, cut into square pieces (18 mm in length, 8 mm in width), (iii)–(iv) 0.3 mm thick FEP films sprayed with conductive ink serving as a dielectric layer, (v) an intermediate 1 mm thick CPP, and (vi) a top 2 mm thick silicone layer with an array of spinosums. The flexible cover and flexible support are made of Dragonskin 30. Specifically, 30 ml part A and 30 ml part B of silicone rubber are mixed in a petri dish. Then, a vacuum pump is used to vacuum the mixture to 0.1 MP for 2.5 min. When the evacuation of the mixture is finished, the mixture is poured into a mold manufactured by 3D printing. The molds of the upper hatch cover and fixed frame made from polylactic acid are also manufactured by 3D printing. In addition, The conductive ink No. is CH-8(MOD2) that is

produced by JUJO printing supplies and technology (Pinghu) Co. Ltd. The conductive ink is printed on the FEP membrane by the screen-printing technology, then dried in the atmosphere temperature. Finally, the flexible cover, fixed frame, and upper hatch cover parts are assembled using an elastomeric O-Ring seal and several screws.

Electric measurement and characterization

Field-emission scanning electron microscopy (Hitachi SU8010) is used to characterize the surface morphology of the nanostructured FEP film sprayed with conductive ink. For the electric output measurement of the TPTS, a linear motor (LINMOT EI200-P01) with a frequency modulation program is used to drive the pressure sensor (LZ-WL2) to collision for quantified investigation. A Keithley (6514) electrometer is adopted to measure the voltage signal. NI-6259 is used for data collection. The software platform is constructed on the basis of LabVIEW, which is capable of realizing real-time data acquisition control and analysis. For example, an intelligent display instrument shows the simulated external load generated by changing the setting parameters of the linear motor. When the TPTS collides with the pressure sensor formed by the linear motor, the Keithley electrometer samples the electric signal and transmits the data to the computer for visualization with LabVIEW software.

DATA AVAILABILITY

The datasets generated during and/or analyzed during the current study are available from the corresponding author on reasonable request.

Received: 5 December 2021; Accepted: 20 March 2022;

Published online: 25 April 2022

REFERENCES

- Paull, L., Saeedi, S., Seto, M. & Li, H. Sensor-driven online coverage planning for autonomous underwater vehicles. *IEEE ASME Trans Mechatron.* **18**, 1827–1838 (2012).
- Melo, J. & Matos, A. Survey on advances on terrain based navigation for autonomous underwater vehicles. *Ocean Eng.* **139**, 250–264 (2017).
- He, B. et al. Autonomous navigation for autonomous underwater vehicles based on information filters and active sensing. *Sens.* **11**, 10958–10980 (2011).
- Jakuba, M. V. et al. Toward automatic classification of chemical sensor data from autonomous underwater vehicles. In *2011 IEEE/RSJ International Conference on Intelligent Robots and Systems.* 4722–4727 (2011).
- Lin, Y. H., Shou, K. P. & Huang, L. J. The initial study of IIS-based binocular stereo-vision system on underwater 3D image reconstruction in the laboratory. *J. Mar. Sci. Technol.* **22**, 513–532 (2017).
- Bruno, F., Bianco, G., Muzzupappa, M., Barone, S. & Rationale, A. V. Experimentation of structured light and stereo vision for underwater 3D reconstruction. *ISPRS J. Photogramm. Remote Sens.* **66**, 508–518 (2011).
- Dimitratos, S. D. et al. Biosensors to monitor water quality utilizing insect odorant-binding proteins as detector elements. *Biosensors.* **9**, 62 (2019).
- Kröger, S. & Law, R. J. Biosensors for marine applications: We all need the sea, but does the sea need biosensors? *Biosens. Bioelectron.* **20**, 1903–1913 (2005).
- Grenon, G., An, P. E., Smith, S. M. & Healey, A. J. Enhancement of the inertial navigation system for the morpheus autonomous underwater vehicles. *J. Ocean. Eng.* **26**, 548–560 (2001).
- Panish, R. & Taylor, M. Achieving high navigation accuracy using inertial navigation systems in autonomous underwater vehicles. In *OCEANS 2011 1–7* (IEEE, Spain, 2011).
- Lee, P. M. & Jun, B. H. Pseudo long base line navigation algorithm for underwater vehicles with inertial sensors and two acoustic range measurements. *Ocean Eng.* **34**, 416–425 (2007).
- Rooney, T., Pipe, A. G., Dogramadzi, S. & Pearson, M. Towards tactile sensing applied to underwater autonomous vehicles for near shore survey and demining. In *Conference Towards Autonomous Robotic Systems.* 463–464 (2012).
- Muscolo, G. G. & Cannata, G. A novel tactile sensor for underwater applications: limits and perspectives. In *OCEANS 2015-Genova.* 1–7 (2015).
- Yohan, N. et al. A three-axial body force sensor for flexible manipulators. In *2014 IEEE International Conference on Robotics and Automation (ICRA).* 6388–6393 (2014).
- Sun, Y., Liu, F., Yuan, Z. P., Huang, W., M. & Wang, B. W. A novel three-axial force tactile sensor based on the fringing effect of electric field. *IEEE Trans. Magn.* **55**, 1–5 (2019).
- Ju, F. et al. A miniature piezoelectric spiral tactile sensor for tissue hardness palpation with catheter robot in minimally invasive surgery. *Smart Mater. Struct.* **28**, 025033 (2019).
- Dehnhardt, G. & Mauck, B. Mechanoreception in secondarily aquatic vertebrates. In *Sensory evolution on the threshold.* 295–314 (2008).
- Niesterok, B., Kruger, Y., Wieskotten, S., Dehnhardt, G. & Hanke, W. Hydrodynamic detection and localization of artificial flatfish breathing currents by harbour seals (*phoca vitulina*). *J. Exp. Biol.* **220**, 174–185 (2017).
- Strobel, S. M., Sills, J. M., Tinker, M. T. & Reichmuth, C. J. Active touch in sea otters: in-air and underwater texture discrimination thresholds and behavioral strategies for paws and vibrissae. *J. Exp. Biol.* **221**, jeb181347 (2018).
- Beem, H., Hildner, M. & Triantafyllou, M. Characterization of a harbor seal whisker-inspired flow sensor. In *2012 Oceans.* 1–4 (2012).
- Beem, H., Liu, Y., Barbastathis, G. & Triantafyllou, M. Vortex-induced vibration measurements of seal whiskers using digital holography. In *OCEANS 2014-TAIPEI.* 1–4 (2014).
- Wegiriya, H., Herzog, N., Abad, S. A., Sadati, S. H. & Nanayakkara, T. A stiffness controllable multimodal whisker sensor follicle for texture comparison. *IEEE Sens. J.* **20**, 2320–2328 (2019).
- Fan, F. R., Tian, Z.-Q. & Wang, Z. L. Flexible triboelectric generator. *Nano Energy.* **1**, 328–334 (2012).
- Xia, X., Fu, J. J. & Zi, Y. L. A universal standardized method for output capability assessment of nanogenerators. *Nat. Commun.* **10**, 4428 (2019).
- Wang, H., Cheng, J., Wang, Z. Z., Ji, L. H. & Wang, Z. L. Triboelectric nanogenerators for human-health care. *Sci. Bull.* **66**, 490–511 (2020).
- Xie, W. B. et al. A nonresonant hybridized electromagnetic-triboelectric nanogenerator for irregular and ultralow frequency blue energy harvesting. *Research.* <https://doi.org/10.34133/2021/5963293> (2021).
- Wang, Z. L., Jiang, T. & Xu, L. Toward the blue energy dream by triboelectric nanogenerator networks. *Nano Energy.* **39**, 9–23 (2017).
- Shi, Q., Wang, H., Wu, H. & Lee, C. K. Self-powered triboelectric nanogenerator buoy ball for applications ranging from environment monitoring to water wave energy farm. *Nano Energy.* **40**, 203–213 (2017).
- Shi, Q. F., Wu, H., Wang, H., Wu, H. X. & Lee, C. K. Self-powered gyroscope ball using a triboelectric mechanism. *Adv. Energy Mater.* **7**, 1701300 (2017).
- Guo, H. et al. A highly sensitive, self-powered triboelectric auditory sensor for social robotics and hearing aids. *Sci. Robot.* **3**, eaat2516 (2018).
- He, Q. et al. Triboelectric vibration sensor for a human-machine interface built on ubiquitous surfaces. *Nano Energy.* **59**, 689–696 (2019).
- Jin, T. et al. Triboelectric nanogenerator sensors for soft robotics aiming at digital twin applications. *Nat. Commun.* **11**, 5381 (2020).
- Xu, P. et al. A triboelectric-based artificial whisker for reactive obstacle avoidance and local mapping. *Research.* **2021**, 9864967 (2021).
- Luo, Y. et al. Triboelectric bending sensor based smart glove towards intuitive multi-dimensional human-machine interfaces. *Nano Energy.* **89**, 106330 (2021).
- Li, J. R. et al. Triboelectric nanogenerators enabled internet of things: a survey. *Intelligent Converged Netw.* **1**, 115–141 (2020).
- Kumar, K. S. et al. Stretchable capacitive pressure sensing sleeve deployable onto catheter balloons towards continuous intra-abdominal pressure monitoring. *Biosensors.* **11**, 156 (2021).
- Wu, Z. Y. et al. Multifunctional sensor based on translational-rotary triboelectric nanogenerator. *Adv. Energy Mater.* **9**, 1901124 (2019).
- Cheng, B. L. et al. Mechanically asymmetrical triboelectric nanogenerator for self-powered monitoring of in vivo microscale weak movement. *Adv. Energy Mater.* **10**, 2000827 (2020).
- Bicchi, A., Salisbury, K. J. & Brock, D. L. Contact sensing from force measurements. *Int. J. Robot. Res.* **12**, 249–262 (1993).

ACKNOWLEDGEMENTS

The authors would like to thank the National Key R & D Project from the Minister of Science and Technology (2021YFA1201604), the Dalian Outstanding Young Scientific and Technological Talents Project (2021RJ11), the National Natural Science Foundation of China (62003175, 51879022), the Beijing Natural Science Foundation (No. 4192026), and the Academy of Finland (Grant No. 315660).

AUTHOR CONTRIBUTIONS

M.X. designed the experiments. J.L. and X.L. synthesized the targets. P.X., J.L., and X.L. performed sample growth. P.X., J.L., X.W., and S.W. performed magnetism measurements. P.X., J.L., X.L., J.Z., and T.C. performed sample structural characterization and data analysis. H.W. and C.W. performed theoretical calculations. P.X. wrote the manuscript with significant contributions from J.L., X.W., J.Z., T.C., H.W., and C.W.

as well as contributions from all other authors. M.X., J.T., and G.X. supervised the project.

COMPETING INTERESTS

The authors declare no competing interests.

ADDITIONAL INFORMATION

Supplementary information The online version contains supplementary material available at <https://doi.org/10.1038/s41528-022-00160-0>.

Correspondence and requests for materials should be addressed to Guangming Xie, Jin Tao or Minyi Xu.

Reprints and permission information is available at <http://www.nature.com/reprints>

Publisher's note Springer Nature remains neutral with regard to jurisdictional claims in published maps and institutional affiliations.



Open Access This article is licensed under a Creative Commons Attribution 4.0 International License, which permits use, sharing, adaptation, distribution and reproduction in any medium or format, as long as you give appropriate credit to the original author(s) and the source, provide a link to the Creative Commons license, and indicate if changes were made. The images or other third party material in this article are included in the article's Creative Commons license, unless indicated otherwise in a credit line to the material. If material is not included in the article's Creative Commons license and your intended use is not permitted by statutory regulation or exceeds the permitted use, you will need to obtain permission directly from the copyright holder. To view a copy of this license, visit <http://creativecommons.org/licenses/by/4.0/>.

© The Author(s) 2022